nature materials

Article

https://doi.org/10.1038/s41563-024-01865-5

A DNA origami device spatially controls CD95 signalling to induce immune tolerance in rheumatoid arthritis

Received: 29 May 2022

Accepted: 15 March 2024

Published online: 09 April 2024

Check for updates

Ling Li[1,9], Jue Yin[2,9], Wen Ma[3,9], Longguang Tang[4,9], Jianhua Zou[5,6,7], Linzi Yang[2], Ting Du[1], Yi Zhao[3], Lianhui Wang[2], Zhen Yang[3] ✉, Chunhai Fan[8], Jie Chao[2] ✉ & Xiaoyuan Chen[5,6,7] ✉

DNA origami is capable of spatially organizing molecules into sophisticated geometric patterns with nanometric precision. Here we describe a reconfigurable, two-dimensional DNA origami with geometrically patterned CD95 ligands that regulates immune cell signalling to alleviate rheumatoid arthritis. In response to pH changes, the device reversibly transforms from a closed to an open configuration, displaying a hexagonal pattern of CD95 ligands with ~10 nm intermolecular spacing, precisely mirroring the spatial arrangement of CD95 receptor clusters on the surface of immune cells. In a collagen-induced arthritis mouse model, DNA origami elicits robust and selective activation of CD95 death-inducing signalling in activated immune cells located in inflamed synovial tissues. Such localized immune tolerance ameliorates joint damage with no noticeable side effects. This device allows for the precise spatial control of cellular signalling, expanding our understanding of ligand–receptor interactions and is a promising platform for the development of pharmacological interventions targeting these interactions.

Rheumatoid arthritis (RA) is a systemic autoimmune disease that affects polyarticular joints. The inflammatory process is characterized by infiltration of various inflammatory/immune cells (including T cells, B cells and macrophages)[1,2] into the synovial hyperplasia, leading to progressive destruction of joints and bone. Despite the rapid development of new treatment regimens, long-term disease remission without severe side effects has not yet been achieved for most patients with RA. Effective treatment of RA may require the elimination of most activated immune cells in the inflamed synovial tissues to blunt autoimmune responses. The CD95/CD95 ligand

[1]West China School of Public Health and West China Fourth Hospital, and State Key Laboratory of Biotherapy, Sichuan University, Chengdu, China. [2]Key Laboratory for Organic Electronics and Information Displays & Jiangsu Key Laboratory for Biosensors, Institute of Advanced Materials, National Synergetic Innovation Center for Advanced Materials, Nanjing University of Posts and Telecommunications, Nanjing, China. [3]Strait Laboratory of Flexible Electronics, Fujian Key Laboratory of Flexible Electronics, Strait Institute of Flexible Electronics, Fujian Normal University, Fuzhou, China. [4]Department of Pharmacy, Center for Regeneration and Aging Medicine, the Fourth Affiliated Hospital of School of Medicine, and International School of Medicine, International Institutes of Medicine, Zhejiang University, Yiwu, China. [5]Departments of Diagnostic Radiology, Surgery, Chemical and Biomolecular Engineering and Biomedical Engineering, Yong Loo Lin School of Medicine and College of Design and Engineering, National University of Singapore, Singapore, Singapore. [6]Clinical Imaging Research Centre, Centre for Translational Medicine, Yong Loo Lin School of Medicine, National University of Singapore, Singapore, Singapore. [7]Nanomedicine Translational Research Program, NUS Center for Nanomedicine, Yong Loo Lin School of Medicine, National University of Singapore, Singapore, Singapore. [8]School of Chemistry and Chemical Engineering, Frontiers Science Center for Transformative Molecules and National Center for Translational Medicine, Shanghai Jiao Tong University, Shanghai, China. [9]These authors contributed equally: Ling Li, Jue Yin, Wen Ma, Longguang Tang. ✉e-mail: ifezhyang@fjnu.edu.cn; iamjchao@njupt.edu.cn; chen.shawn@nus.edu.sg

https://doi.org/10.1038/s41563-024-01865-5

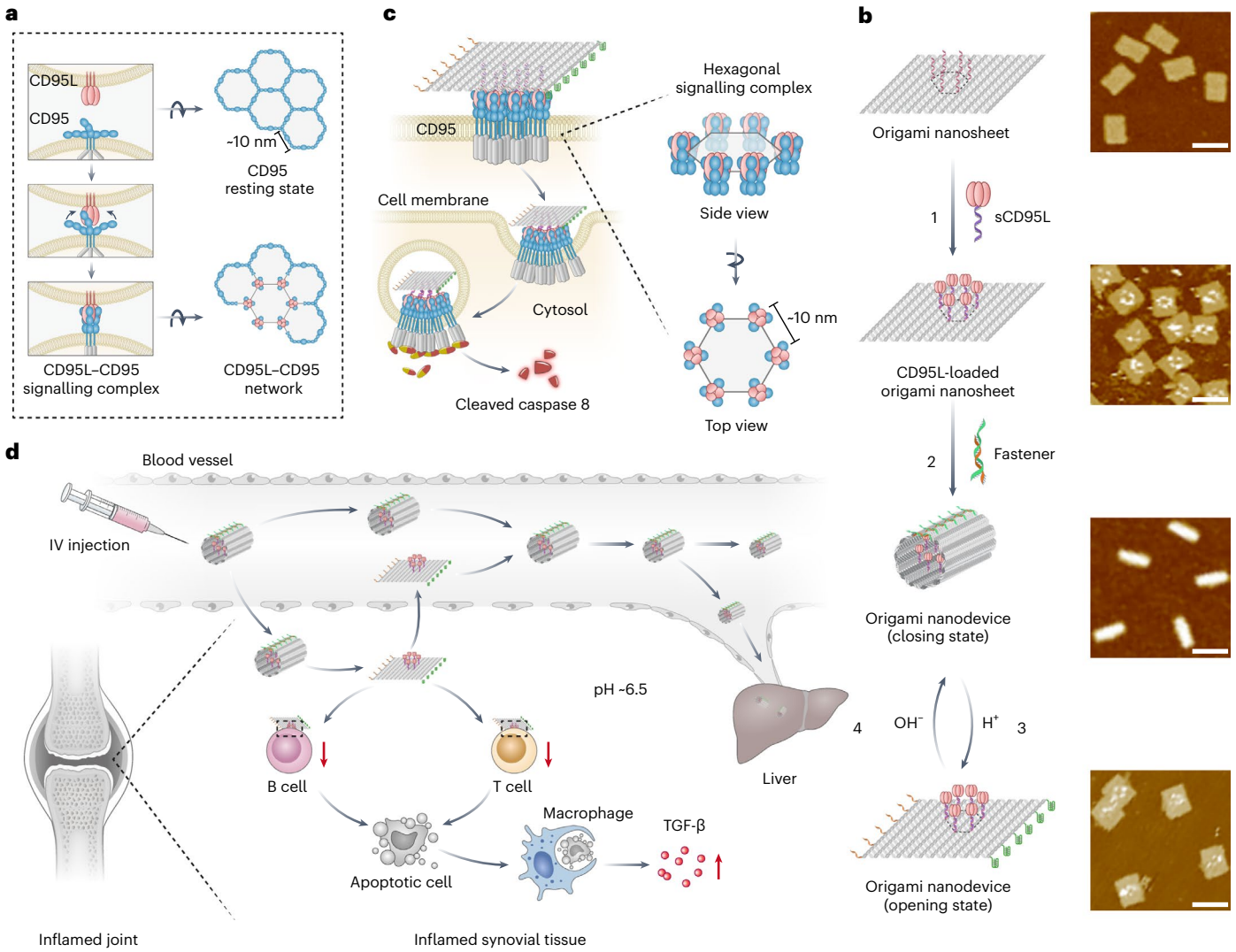

Fig. 1 | Schematic and characterization of designer DNA origami in spatial control of CD95 signalling for reversal of RA. a, Schematic illustration of the model of CD95 receptor resting state based on the hexagonal antiparallel dimer network described by Vanamee and Faustman[4]. **b**, Schematic showing construction of the designer DNA origami nanodevice: (1) the rectangular DNA origami nanosheet with poly-A strand overhang was hybridized with CD95L-poly-T conjugates to form the DNA origami nanosheet with a hexagonal CD95L array pattern. (2) I-motif-based fasteners were applied to lock the DNA origami nanosheet to form the DNA origami nanodevice with the CD95L array on the inner surface. (3) Under acidic conditions (pH 6.5) the DNA origami nanodevice transformed into the opening structure to expose the inner CD95L array in response to the pH-switchable structural transformation of fasteners. (4) With pH increased to 7.4, the opened DNA origami nanodevice reassembled into the closing structure to shield the CD95L array. AFM images are representative of three independent experiments; scale bars, 100 nm. **c**, Schematic showing the process of CD95 signalling activation mediated by the DNA origami nanodevice (opening structure) with a hexagonal CD95L array pattern. **d**, Following intravenous (IV) administration, the DNA origami nanodevice efficiently accumulated in inflamed synovial tissue owing to oedema and neovascularization in the inflamed joints. The DNA origami nanodevice then transformed into the opening structure to expose the inner CD95L array in the acidic microenvironment. The exposed CD95L array bound to CD95 receptors on activated B and T lymphocytes and induced apoptosis of those cells. This was followed by efferocytosis, which triggered the release of immunosuppressive cytokine TGF-β to quench inflammation and induce localized immune tolerance in the inflamed joints. Meanwhile, some of the opened DNA origami nanodevices in the inflamed joints that did not bind to the CD95 receptors may have re-entered the bloodstream, where they would have undergone structural transformation and reassembly into the closing structure, thereby sparing hepatocytes and thus minimizing liver damage.

(CD95L) signalling pathway plays crucial roles in the elimination of activated lymphocytes and induction of immune tolerance to self-antigens[3]. Activation of CD95 death-inducing signalling to induce apoptosis of activated immune cells in inflamed joints holds great potential for the establishment of localized immune tolerance for reversal of RA.

It has been demonstrated that transmembrane CD95 receptors are prearranged in a 'non-signalling' resting state in hexagonal patterns and, following binding of CD95L, they are further arranged in hexameric supramolecular clusters with an intermolecular distance of approximately 10 nm to assemble intracellular complexes for signalling transduction[4,5] (Fig. 1a). Efficient activation of CD95 death-inducing signalling requires hexameric or membrane-bound CD95L with an optimal intermolecular spacing of approximately 10 nm[4,6,7]. Although previous studies have shown that some synthetic scaffolds (polymers, dendrimers, nanofibres and so on) have been employed to elucidate cellular signalling behaviour, these offer limited control over ligand spacing, valency and spatial arrangements. As an alternative, designer DNA origami can be programmed to provide sophisticated geometric patterns of ligand array with nanometric precision[8–17], thereby

enabling precise modulation of cellular signalling and subsequent cellular responses.

Herein we describe a strategy that utilizes a programmable DNA origami to regulate CD95 death-inducing signalling of activated immune cells in inflamed synovial tissues to establish localized immune tolerance for RA reversal. This DNA origami was designed to display CD95L array in a two-dimensional hexagonal pattern with approximately 10 nm intermolecular spacing, fitting well with the geometric arrangement of transmembrane CD95 receptor clusters (Fig. 1b,c). I-motif DNA sequence-based fasteners were further coupled to the DNA origami to enable reversible closing and opening transition of conformation in response to a pH trigger. The designer DNA origami maintained closing configuration under neutral conditions and transformed into the opening configuration to expose the hexagonal pattern of the CD95L array in a weakly acidic environment. This feature greatly enhanced selective activation of CD95 death-inducing signalling in activated immune cells in inflamed synovial tissues (pH ~6.5)[18–20] while sparing healthy hepatocytes expressing low levels of CD95 receptors in the liver[21] (pH ~7.4), thereby minimizing hepatotoxicity (Fig. 1d). We demonstrate that, in a collagen-induced arthritis (CIA) mouse model, local ablation of immune cells in inflamed synovial tissues significantly alleviated chronic inflammation, promoted localized immune tolerance and ameliorated joint damage with no noticeable side effects.

Construction of the designer DNA origami

Initially the base design for the programmable DNA origami was a rectangular DNA origami nanosheet (referred to as NS-empty) of dimensions 90 × 60 × 2 nm^3, which was constructed by assembling an M13 circular DNA scaffold with multiple staple strands[22,23] (Supplementary Fig. 1). To anchor CD95L into a hexagonal pattern we modified this base design to display six sets of protruding, single-stranded poly-A strands. CD95L, which spontaneously forms the homotrimer, was conjugated to the end of single-stranded poly-T strands designed to hybridize with poly-A overhangs on the surface of the DNA origami nanosheet (Fig. 1b and Supplementary Figs. 2 and 3). To investigate the effect of CD95L nanoscale spacing on CD95 receptor activation, three sets of DNA origami nanosheets were developed to display CD95L at 5, 10 and 30 nm intermolecular distance (hereafter referred to as NS-5, NS-10 and NS-30, respectively; Fig. 2d,e and Supplementary Figs. 4–7). Atomic force microscopy (AFM) imaging revealed that approximately 70% of the DNA origami nanosheet contained six anchored CD95L molecules for NS-10 and NS-30 (Supplementary Fig. 8), demonstrating efficient CD95L capture at each binding site. For spatial control of the activity of the CD95L array, six pairs of i-motif DNA sequence-based fasteners were further applied to lock the DNA origami nanosheet into forming a nanodevice. These fasteners exhibited dynamic pH-switchable structural transformation (Supplementary Figs. 9–11), thereby enabling the resulting DNA origami nanodevice with reversible closing and opening features (Fig. 2a–c). Under neutral conditions (pH ~7.4), the DNA origami nanodevice was assembled into the closing structure thereby shielding the CD95L array on the inner surface. By contrast, with pH decreased to 6.5 the nanodevice showed a full opening structure to expose the inner CD95L array.

Both ionic strength and nucleases in biological fluids have a major effect on the stability of DNA origami nanostructures[24–28]. We next examined the effect of magnesium ion (Mg^{2+}), pH and nuclease on the integrity of DNA origami nanostructures. We found that the structures of both DNA origami nanosheets and nanodevices remained fully intact following incubation in buffer with Mg^{2+} concentration at 1.0 mM (similar to that in the blood) for either 12 or 24 h (Supplementary Figs. 12–14). In addition, no substantial disintegration of DNA origami nanostructure was observed in buffer at pH 7.4, 6.5 or 5.0 (Supplementary Fig. 15). Although mounting evidence suggests that DNA origami nanostructures exhibit enhanced resistance to nucleases[29,30], some evidence of degradation was found in the presence of DNase I (Supplementary Fig. 16). Compared with the DNA origami nanosheet, the DNA origami nanodevice appeared more stable in the buffer with DNase I, attributed probably to a reduction in binding to this enzyme. Similar results were observed in buffer with non-inactivated serum (Supplementary Figs. 17 and 18). Importantly, the dynamic conformational transition of the DNA origami nanodevice in response to pH trigger was detected in the buffer with non-inactivated serum (Supplementary Fig. 19).

Designer DNA origami regulates CD95 signalling transduction

To investigate whether the nanoscale arrangement of the CD95L array affects CD95 signalling initiation, we examined the apoptosis effect in A20 (B lymphocyte cell line) and Jurkat (T lymphocyte cell line) cells following treatment with either NS-5, NS-10 or NS-30. We observed that soluble CD95L (sCD95L) did not induce apoptosis in Jurkat cells even at concentrations as high as 500 ng ml^{-1} (Fig. 2f). In A20 cells, which are more sensitive to CD95L-mediated apoptosis, sCD95L showed only a slight increase in activity. These results indicated that the soluble form of CD95L is somewhat inactive and exhibits minimal apoptosis-inducing ability, in agreement with a previous study[31]. In sharp contrast to this, organization of sCD95L on the DNA origami nanosheet to form a CD95L array markedly increased its activity. Both NS-5 (half-maximal effect (EC_{50}), 9.57 ng ml^{-1}) and NS-30 (EC_{50}, 11.23 ng ml^{-1}) led to a substantial increase in the fraction of apoptotic A20 cells. Interestingly, NS-10 (EC_{50}, 5.00 ng ml^{-1}) was more efficient at inducing apoptosis than either NS-5 or NS-30 in A20 cells. Analysis of Jurkat cells following treatment revealed similar results (Fig. 2f). NS-10 (EC_{50}, 12.23 ng ml^{-1}) led to a sevenfold increase in the fraction of apoptotic Jurkat cells compared with both NS-5 (EC_{50}, 97.19 ng ml^{-1}) and NS-30 (EC_{50}, 104.30 ng ml^{-1}). These results indicate that the nanometric spatial arrangements of CD95L tune the apoptosis-inducing effect. This finding is in line with ligand–receptor complex models of the tumour necrosis factor (TNF) superfamily to which CD95 and CD95L belong[5,7]. NS-10, with a CD95L array pattern precisely matching this ligand–receptor complex model, exhibited maximal potency. Next we sought to investigate the apoptosis-inducing effect of ND-10 (DNA origami nanodevice with CD95L at 10 nm intermolecular distance). Negligible apoptosis was detected following ND-10 treatment under neutral conditions (Fig. 2g). However, under acidic conditions, ND-10 markedly enhanced apoptosis in both A20 and Jurkat cells (Supplementary Fig. 20), with EC_{50} comparable to that of NS-10.

According to the current model of CD95 signalling, binding of active CD95L induces aggregation of CD95 receptors at the cell surface to initiate signalling transduction[32,33] (Fig. 3a). To uncover the mechanism underlying the superior performance of NS-10, we next investigated CD95 receptor distribution following NS-10 stimulation. We observed that A20 cells showed higher-order clustering of CD95 under NS-10 treatment (Fig. 3b). Following 2 h of NS-10 stimulation, CD95 receptor distribution changed to a highly clustered spot pattern; by contrast, treatment with NS-empty or sCD95L did not induce detectable changes in CD95 distribution. The effect of ND-10 on CD95 receptor distribution was also monitored. Under neutral conditions, CD95 receptor distribution showed no sign of clustering following ND-10 treatment, further confirming the shielding effect of the nanodevice (Fig. 3b). In comparison, ND-10 mediated a marked increase in the magnitude of CD95 receptor clustering under acidic conditions. These treatments revealed similar results in Jurkat cells (Extended Data Fig. 1a).

In general, the clustering of CD95 receptors is followed by endocytosis, which leads to activation of downstream signalling (Fig. 3a). It was observed that many of the spot patterns of CD95 receptors following NS-10 stimulation appeared to be cytoplasmic rather than being clustered on the cell surface (Fig. 3b). To this end, we further investigated endocytosis of receptors in response to NS-10 treatment. Most CD95 receptors in A20 cells were internalized and translocated to early

https://doi.org/10.1038/s41563-024-01865-5

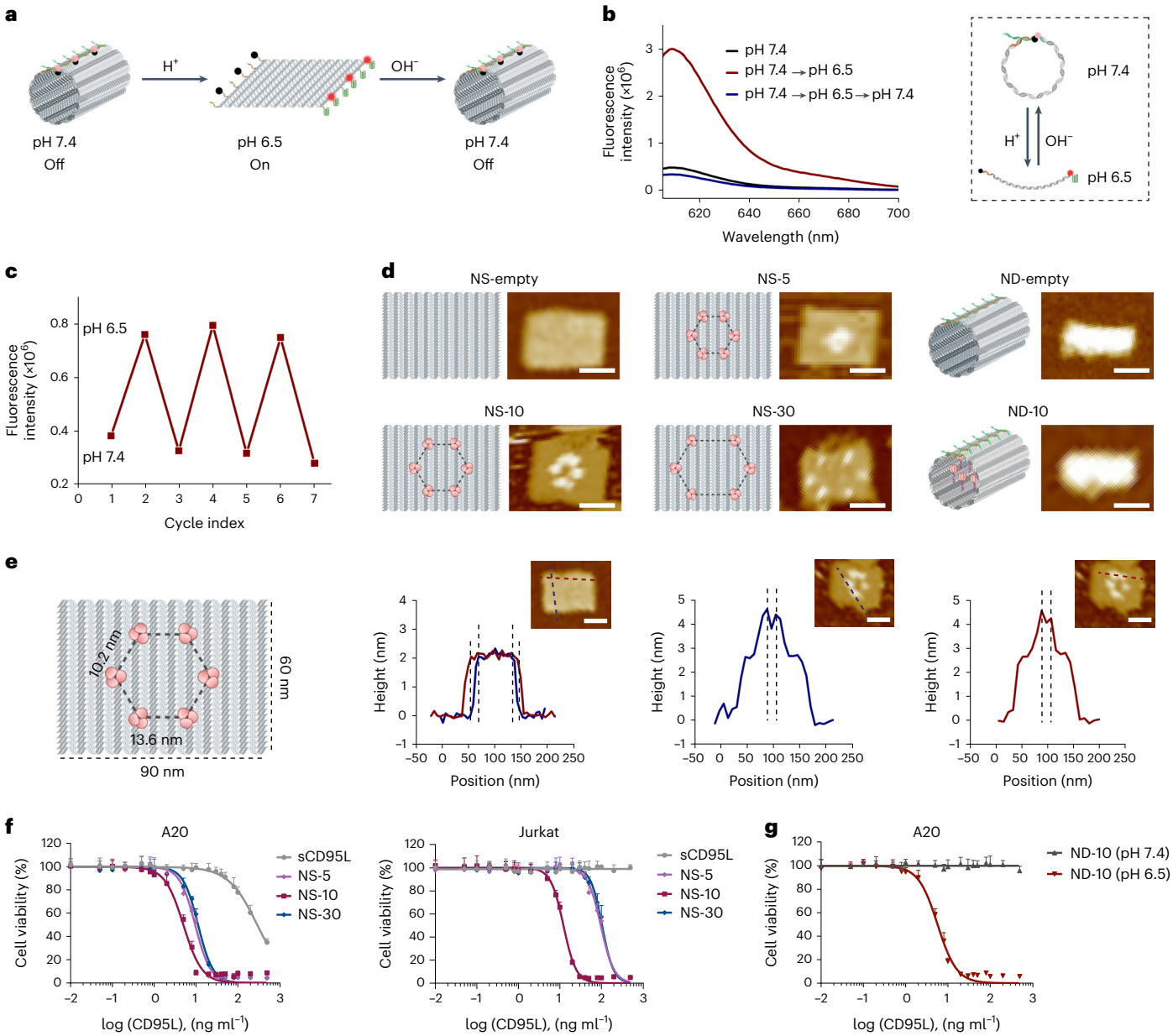

Fig. 2 | Characterization of the designer DNA origami. a, Schematic showing the opening–closing conformational transition of the designer DNA origami. The i-motif strand of the fastener was labelled with Texas Red fluorophore, and the complementary strand with BHQ2 quencher. **b**, pH-dependent fluorescence emission spectra of the designer DNA origami in buffer under varying pH. **c**, Fluorescence intensity of the designer DNA origami following repeat pH switching between 7.4 and 6.5. **d**, Schematic and representative AFM images of NS-empty, NS-5, NS-10, NS-30, ND-empty and ND-10; scale bars, 50 nm. The experiment was performed five times, with similar results. **e**, Measurement of the size of NS-10 and distances between CD95L molecules; scale bars, 50 nm. **f**, In vitro cytotoxicity (CCK-8 assay) of sCD95L, NS-5, NS-10 and NS-30 in A20 and Jurkat cells; $n = 6$ biologically independent samples. The experiment was performed three times, with similar results. **g**, In vitro cytotoxicity (CCK-8 assay) of ND-10 in culture medium (pH 7.4 or 6.5) in A20 cells; $n = 6$ biologically independent samples. The experiment was performed three times, with similar results. **f**,**g**, Data presented as means ± s.d.

endosomes 2 h following NS-10 stimulation (Fig. 3c). Similarly, under acidic conditions, ND-10 induced receptor endocytosis at levels comparable to those following NS-10 stimulation (Supplementary Fig. 21). Analysis of Jurkat cells revealed similar results (Extended Data Fig. 1b,c). Dynamin inhibition substantially hampered the endocytosis of CD95 receptors in NS-10-treated cells (Supplementary Figs. 22 and 23), indicating that dynamin plays a prominent role in CD95 endocytosis following NS-10 stimulation. These findings suggest that NS-10 stimulation results in internalization of receptor–ligand complexes following CD95 receptor clustering, which are then directed towards an endosomal pathway.

To determine whether endocytosis of receptor–ligand complexes could initiate signalling transduction, we examined downstream caspase 8 activation. The results showed that neither NS-empty nor sCD95L led to upregulation of cleaved caspase 8 expression in A20 or Jurkat cells (Fig. 3d, Extended Data Fig. 1d and Supplementary Fig. 24). By contrast, the expression of cleaved caspase 8 was substantially enhanced following NS-10 treatment, demonstrating that the internalization of receptor–ligand complexes triggers downstream signalling. NS-10 treatment led to extensive cell apoptosis, and ND-10 induced cell apoptosis at a comparable level, under acidic conditions (Supplementary Fig. 25). Furthermore, these apoptotic

https://doi.org/10.1038/s41563-024-01865-5

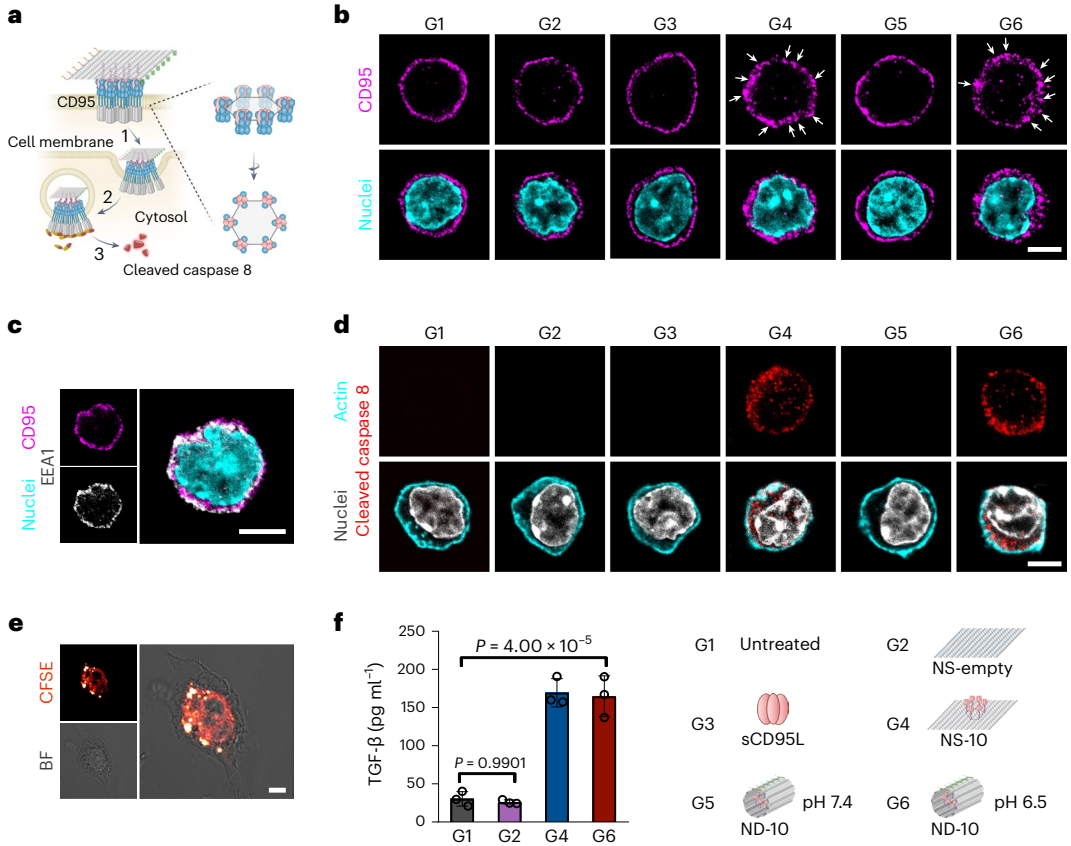

Fig. 3 | Spatial arrangement of the CD95L array directs the activation of CD95 signalling in A20 cells. a, Schematic showing the process of CD95 signalling activation. Hexagonal CD95L array binding to CD95 receptors via precise spatial pattern recognition induced higher-order clustering of CD95 receptors (1), followed by internalization of these ligand–receptor complexes through the endosomal pathway (2); the death-inducing signalling complex was then recruited to this compartment to transduce downstream signalling (3). **b**, Clustering of CD95 receptors in A20 cells at 2 h following treatment with NS-empty (G2), sCD95L (G3), NS-10 (G4), ND-10 in culture medium (pH 7.4) (G5) and ND-10 in culture medium (pH 6.5) (G6), and untreated (G1); scale bar, 5 μm. **c**, Colocalization of CD95 receptors with the endosomal marker EEA1 following NS-10 stimulation. A20 cells were stimulated for 2 h with NS-10; scale bar, 5 μm. **d**, Immunocytochemical analysis of cleaved caspase 8 in A20 cells 6 h following treatment shown in **b**; scale bar, 5 μm. **e**, Representative images of phagocytic clearance of apoptotic A20 cells by BMDMs. A20 cells labelled with carboxyfluorescein succinimidyl ester (CFSE) fluorophore were treated with ND-10 in culture medium (pH 6.5); BMDMs were added to the medium following treatment, with coculture for a further 0.5 h; scale bar, 5 μm. Experiments were performed three times, with similar results. BF, bright field. **f**, Concentration of TGF-β in supernatants following the indicated treatments; $n = 3$ biologically independent samples per group. The experiment was performed three times, with similar results. G1, BMDMs were cocultured with untreated A20 cells; G2, BMDMs were cocultured with A20 cells pretreated with NS-empty; G4, BMDMs were cocultured with A20 cells pretreated with NS-10; G6, BMDMs were cocultured with A20 cells pretreated with ND-10 in culture medium (pH 6.5). Data presented as means ± s.d.; statistical significance was calculated via one-way ANOVA with Tukey post hoc test.

cells are readily phagocytosed by bone marrow-derived macrophages (BMDMs) (Fig. 3e) and promote the release of TGF-β (Fig. 3f), a canonical anti-inflammatory cytokine.

Biodistribution and biosafety of the designer DNA origami

In general, selective accumulation in diseased sites while sparing healthy tissues is ideal for ensuring both efficacy and biosafety. To assess whether the DNA origami nanodevice can efficiently accumulate in inflamed synovial tissue, we established a CIA model in mice. To visualize the distribution of the DNA origami nanodevice in vivo we modified staple strands to contain Cy5.5-labelled poly-A overhangs (imaging strands; referred to as ND-Cy5.5). Near-infrared fluorescence imaging revealed minimal fluorescence signal in the joints and paws of healthy mice following ND-Cy5.5 injection (Fig. 4a and Supplementary Fig. 26). In stark contrast to this, ND-Cy5.5 progressively accumulated in the inflamed joints and paws of CIA mice, peaking at 12 h post injection (Fig. 4a and Supplementary Fig. 27). We reasoned that both oedema and neovascularization in inflamed joints had enhanced the permeation and retention of ND-Cy5.5. Ex vivo imaging further revealed a much stronger fluorescence signal in inflamed joints and paws than that in healthy joints and paws (Fig. 4b,c and Supplementary Fig. 28). We further investigated the conformational transition of the DNA origami nanodevice in response to pH trigger in vivo. Substantial fluorescence signal was detected in the joints and paws of CIA mice at 4 h post injection with the pH-sensitive nanodevice (w/Cy5.5 & BBQ650; Extended Data Fig. 2 and Supplementary Figs. 29–31). By contrast, little to no fluorescence signal was observed in the joints and paws of CIA mice treated with the pH-non-sensitive nanodevice (w/Cy5.5 & BBQ650). These results showed that DNA origami nanostructures effectively accumulated in inflamed tissues and that the pH-triggered conformational transition feature of the DNA origami nanodevice was strongly retained in vivo.

Next we examined whether the DNA origami nanodevice would be capable of shielding the CD95L array from hepatocytes to prevent liver damage. No elevated serum alanine transaminase (ALT) or aspartate aminotransferase (AST) was detected following administration of either ND-empty or ND-10 (Fig. 4d). Liver histology analysis revealed

https://doi.org/10.1038/s41563-024-01865-5

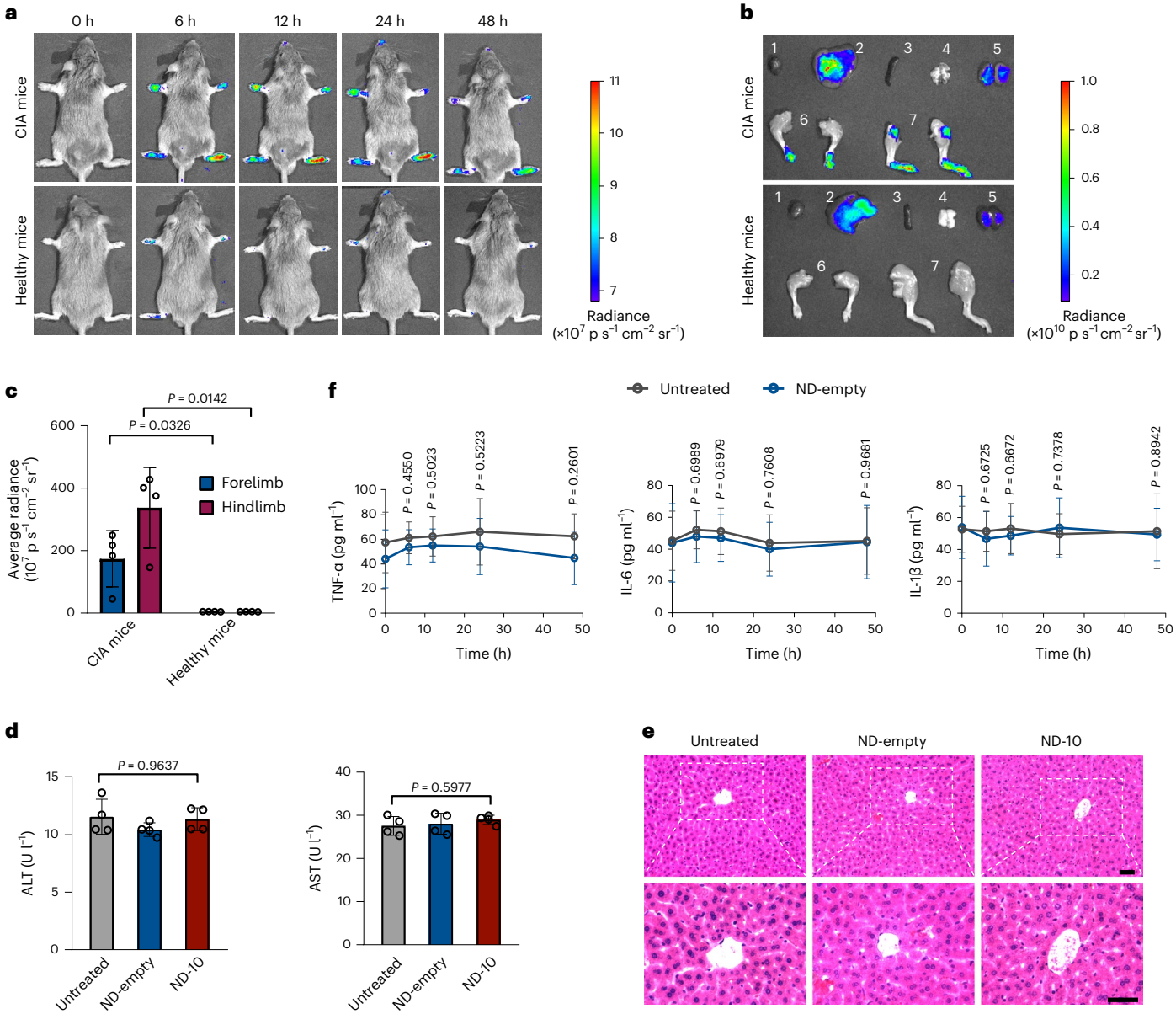

Fig. 4 | In vivo distribution and biosafety of the designer DNA origami in mice. **a**, Representative in vivo fluorescence images of CIA and healthy mice following intravenous injection with ND-Cy5.5. **b**, Representative ex vivo fluorescence images of major organs obtained from mice 24 h post intravenous injection with ND-Cy5.5: 1, heart; 2, liver; 3, spleen; 4, lung; 5, kidney; 6, forelimb; 7, hindlimb. **c**, Fluorescence signal quantification for forelimb and hindlimb obtained from mice 24 h following intravenous injection of ND-Cy5.5; $n = 4$ biologically independent mice per group. **d**, Biochemistry profile (ALT, AST) analysis of healthy mice following the indicated treatments; $n = 4$ biologically independent mice per group. The experiment was performed twice, with similar results. **e**, Histological examination (H&E staining) of liver sections obtained from healthy mice following the indicated treatments; scale bar, 50 μm. **f**, Serum concentrations of TNF-α, IL-6 and IL-1β in healthy mice over a 48 h period following the indicated treatments; $n = 4$ biologically independent mice per group. The experiment was performed twice, with similar results. **c**,**d**,**f**, Data presented as mean ± s.d. Statistical significance was calculated via either two-tailed Student's *t*-test (**c**,**f**) or one-way ANOVA with Tukey post hoc test (**d**).

no sign of liver haemorrhage or hepatocyte apoptosis following ND-10 administration (Fig. 4e). These data demonstrated that the DNA origami nanodevice can indeed shield the inner CD95L array from reaching hepatocytes and thereby preventing liver damage.

Because DNA origami is composed of DNA scaffold and large amounts of DNA staple strands, we next assessed its immunomodulation potential. All DNA origami nanodevice samples had endotoxin levels <10 endotoxin units (EU) ml^{-1} (Supplementary Figs. 32 and 33), satisfying the endotoxin limits in formulations for biomedical applications[34]. ND-empty treatment over the tested range (0.2–2.0 nM) did not induce the production of TNF-α, IL-6 or IL-1β in either RAW 264.7 cells or BMDMs (Extended Data Fig. 3). Following intravenous injection, ND-empty led to a negligible increase in the concentration of serum TNF-α, IL-6 and IL-1β over a 48 h period (Fig. 4f). These results suggested that DNA origami in this study is immunologically inert, consistent with previous reports that nucleic acid nanoparticles used without a delivery carrier are immunoquiescent[35].

Designer DNA origami triggers robust therapeutic efficacy

Rheumatoid arthritis is a multifaceted, immunologically mediated disease involving $CD4^+$ T cells, B cells and monocytes that infiltrate

https://doi.org/10.1038/s41563-024-01865-5

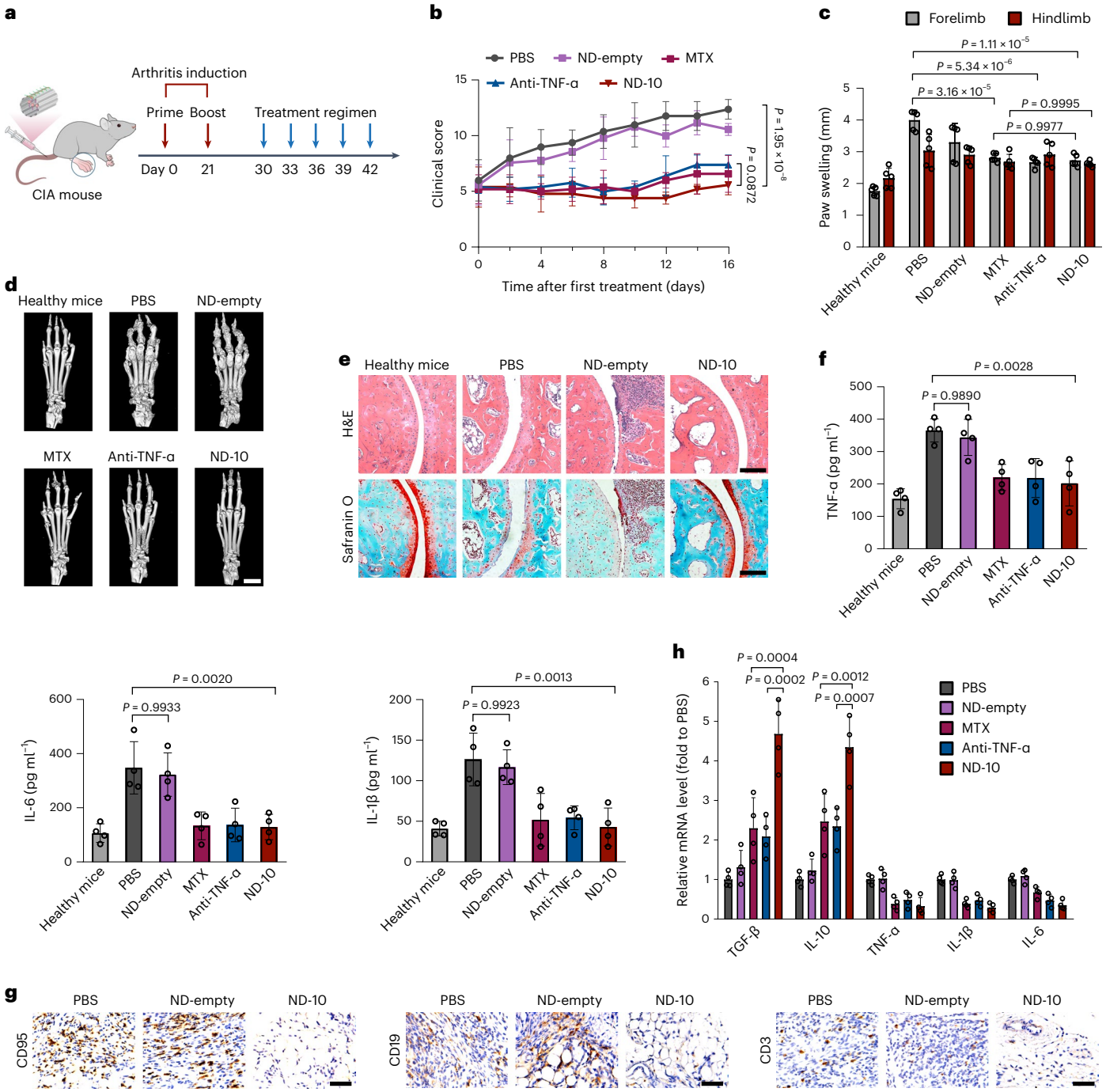

Fig. 5 | Designer DNA origami triggers robust therapeutic efficacy in CIA mice. a, Schematic illustration of the short-term treatment regimen. **b**, Clinical arthritis scores of CIA mice following the indicated treatments; $n = 5$ biologically independent mice per group. The experiment was performed twice, with similar results. **c**, Measurement of paw swelling in CIA mice following the indicated treatments. Healthy mice were used as controls; $n = 5$ biologically independent mice per group. **d**, MicroCT images showing the paws of healthy and CIA mice following the indicated treatments; scale bar, 2 mm. **e**, Histological examination (H&E and Safranin O staining) of joints obtained from healthy and CIA mice following the indicated treatments; scale bars, 100 μm. **f**, Serum concentrations of TNF-α, IL-6 and IL-1β following the indicated treatments; $n = 4$ biologically independent mice per group. **g**, Immunohistochemical analysis of synovial tissues retrieved from mice following the indicated treatments; scale bars, 50 μm. **h**, Relative messenger RNA levels of inflammatory cytokines TNF-α, IL-1β, IL-6, TGF-β and IL-10 in synovial tissues of mice following the indicated treatments; $n = 4$ biologically independent mice per group. **b**,**c**,**f**,**h**, Data presented as means ± s.d.; statistical significance was calculated via one-way ANOVA with Tukey post hoc test.

the synovial tissue and induce pathology. T and B lymphocytes have important roles in the initiation and progression of rheumatoid inflammation[36–38]. We observed substantial enrichment of lymphocytes in inflamed synovial tissue (Supplementary Fig. 34). Following intravenous injection of the DNA origami nanodevice with Cy5 fluorophore labelling (ND-Cy5), a high abundance of both T and B cells was found to be $Cy5^+$ (Supplementary Figs. 35 and 36).

We next evaluated the therapeutic efficacy of the designer DNA origami in CIA mice according to the treatment regimen presented in Fig. 5a. Mice treated with either methotrexate (MTX) or

anti-TNF-α monoclonal antibody (mAb) served as positive controls. As expected, the arthritis score for paws rapidly increased in the PBS group. ND-empty treatment did not alleviate the progression of arthritis (Fig. 5b). In sharp contrast to this, MTX, anti-TNF-α mAb and ND-10 all markedly delayed disease progression, accompanied by a much slower increase in arthritis score. Notably, we observed that the mice showed no weight loss during ND-10 treatment (Supplementary Fig. 37), further confirming the biosafety of ND-10. Paw swelling in mice treated with ND-10 was comparable to that in mice receiving MTX or anti-TNF-α mAb treatment, substantially less than that in the PBS and ND-empty groups (Fig. 5c and Supplementary Fig. 38). Microcomputed tomography (microCT) imaging revealed that the joints of mice in the PBS and ND-empty groups had undergone severe bone erosion (Fig. 5d). Treatment with either MTX, anti-TNF-α mAb or ND-10 markedly suppressed bone erosion, with joint morphology being similar to that of healthy mice. Haematoxylin and eosin (H&E) staining of joints showed serious bone destruction in mice receiving PBS or ND-empty treatment, while those treated with MTX, anti-TNF-α mAb or ND-10 exhibited minimal pathological features (Fig. 5e and Supplementary Fig. 39). Meanwhile, minimal glycosaminoglycan was observed in both the PBS and ND-empty groups, indicating severe degradation of articular cartilage with disease progression. Of note, no signs of cartilage degradation were noted in mice treated with ND-10 (Fig. 5e). In addition, we observed that serum concentrations of TNF-α, IL-1β and IL-6 were significantly elevated in the PBS and ND-empty groups (Fig. 5f). MTX, anti-TNF-α mAb and ND-10 treatment all markedly decreased the concentration of these proinflammatory cytokines to near-normal levels, indicating resolution of arthritis at the systemic level.

Next we investigated immune cell profiles in inflamed synovial tissue. Immunohistochemical analysis showed that massive inflammatory cells expressing CD95 receptors were enriched in the synovial tissue of mice in the PBS group (Fig. 5g and Supplementary Fig. 40). These findings agree with a previous report in which rheumatoid synovial tissue was infiltrated with various inflammatory cells expressing CD95 (refs. 39,40); $CD19^+$ B lymphocytes and $CD3^+$ T lymphocytes were also detected in the synovial tissue of these mice. In sharp contrast to the PBS group, few $CD95^+$ cells, $CD19^+$ B cells or $CD3^+$ T cells were observed in the synovial tissue of mice receiving ND-10 treatment (Fig. 5g and Supplementary Fig. 40). Typically, the proinflammatory cytokines secreted by activated immune cells are critical for RA pathogenesis and progression[41,42]. We next examined inflammatory cytokine profiles in synovial tissue following the inicated treatments. The expression of proinflammatory cytokines considerably decreased in the synovial tissue of mice treated with ND-10 (Fig. 5h). This finding indicates that local ablation of activated immune cells had reduced proinflammatory cytokine levels to ameliorate inflammation in synovial tissue. We also observed that ND-10 treatment induced a substantial increase in the expression of anti-inflammatory cytokines in synovial tissue. Compared with the PBS group, ND-10 treatment elicited a 3.7-fold increase in TGF-β expression and a 3.4-fold increase in IL-10 expression in synovial tissue (Fig. 5h). These findings suggest that the disposal of apoptotic immune cells by phagocytes ('efferocytosis') further established a localized immune tolerance milieu within the joints, in line with previous reports that efferocytosis promotes immune suppression[43,44]. Notably, mice treated with ND-10 showed no elevation in serum levels of ALT or AST (Supplementary Fig. 41) and no evidence of liver damage (Supplementary Fig. 42), probably benefiting from the conformational transition of the DNA origami nanodevice responding to pH trigger.

Encouraged by the substantial elevation of anti-inflammatory cytokines in synovial tissue following ND-10 treatment, we next explored its long-term therapeutic efficacy in a CIA mouse model. Mice were treated every 3 days from days 29–56 (Extended Data Fig. 4a). Both MTX and anti-TNF-α mAb substantially delayed the increase in arthritis score (Extended Data Fig. 4b). Of note, in those mice so treated, arthritis scores increased rapidly following the last treatment. In stark contrast to this, mice treated with ND-10 showed a sustained alleviation of disease following cessation of treatment. At the end of the observation period, paw swelling in mice receiving ND-10 treatment was significantly less than that in both the MTX and anti-TNF-α mAb groups (Extended Data Fig. 4c and Supplementary Fig. 43). These results further support the sustained efficacy of ND-10 treatment in a CIA mouse model.

Discussion

In this study we developed a designer DNA origami-arranging CD95L array into a two-dimensional hexagonal pattern with nanometric precision to regulate CD95 signalling of activated immune cells in inflamed synovial tissues for reversal of RA. We identified that the activation of CD95 signalling is spatially controlled by the nanoscale distribution of CD95L. DNA origami displaying a hexagonal CD95L array with 10 nm intermolecular spacing is optimal to triggering the activation of CD95 signalling due to precise pattern recognition. I-motif DNA sequence-based fasteners were further coupled to DNA origami to render the DNA origami nanodevice with reversible closing and opening features, thereby spatially controlling the activity of the CD95L array in the body. Following systemic administration, ND-10 efficiently accumulated in inflamed joints and specifically exposed the CD95L array to activate CD95 signalling of the activated immune cells in inflamed synovial tissues while sparing healthy hepatocytes, alleviating chronic inflammation and promoting localized immune tolerance in a CIA mouse model.

DNA origami enables the spatial arrangement of molecules into programmable two- or three-dimensional geometric patterns with nanometric precision. Unlike other nanoparticle systems, DNA origami offers flexible control over molecular spacing, valency and spatial arrangements. Mounting evidence suggests that dysregulation of cellular signalling pathways mediates the pathogenesis and progression of many diseases such as cancer and autoimmune disease[45–47]. In this study we used DNA origami as a potent tool in spatial regulation of CD95 signalling for treatment of RA. Our research provides a typical paradigm for spatial regulation of cellular signalling towards the development of pharmacological interventions against disease. The designer DNA origami approach offers a promising strategy for precise spatial control of cellular signalling to expand our understanding of ligand–receptor interaction and develop pharmacological interventions targeting these interactions.

Online content

Any methods, additional references, Nature Portfolio reporting summaries, source data, extended data, supplementary information, acknowledgements, peer review information; details of author contributions and competing interests; and statements of data and code availability are available at https://doi.org/10.1038/s41563-024-01865-5.

References

1. Vital, E. M. & Emery, P. The development of targeted therapies in rheumatoid arthritis. *J. Autoimmun.* **31**, 219–227 (2008).
2. Smolen, J. S. & Aletaha, D. Rheumatoid arthritis therapy reappraisal: strategies, opportunities and challenges. *Nat. Rev. Rheumatol.* **11**, 276–289 (2015).
3. Ju, S.-T. et al. Fas (CD95)/FasL interactions required for programmed cell death after T-cell activation. *Nature* **373**, 444–448 (1995).
4. Vanamee, É. S. & Faustman, D. L. Structural principles of tumor necrosis factor superfamily signaling. *Sci. Signal.* **11**, eaao4910 (2018).
5. Scott, F. L. et al. The Fas–FADD death domain complex structure unravels signalling by receptor clustering. *Nature* **457**, 1019–1022 (2009).

6. Wang, L. et al. The Fas–FADD death domain complex structure reveals the basis of DISC assembly and disease mutations. *Nat. Struct. Mol. Biol.* **17**, 1324–1329 (2010).
7. Balta, G. S. G. et al. 3D cellular architecture modulates tyrosine kinase activity, thereby switching CD95-mediated apoptosis to survival. *Cell Rep.* **29**, 2295–2306 (2019).
8. Rothemund, P. W. Folding DNA to create nanoscale shapes and patterns. *Nature* **440**, 297–302 (2006).
9. Chandrasekaran, A. R., Anderson, N., Kizer, M., Halvorsen, K. & Wang, X. Beyond the fold: emerging biological applications of DNA origami. *ChemBioChem* **17**, 1081–1089 (2016).
10. Shaw, A. et al. Spatial control of membrane receptor function using ligand nanocalipers. *Nat. Methods* **11**, 841–846 (2014).
11. Kwon, P. S. et al. Designer DNA architecture offers precise and multivalent spatial pattern-recognition for viral sensing and inhibition. *Nat. Chem.* **12**, 26–35 (2020).
12. Wang, Y., Baars, I., Fordos, F. & Hogberg, B. Clustering of death receptor for apoptosis using nanoscale patterns of peptides. *ACS Nano* **15**, 9614–9626 (2021).
13. Comberlato, A., Koga, M. M., Nüssing, S., Parish, I. A. & Bastings, M. M. C. Spatially controlled activation of Toll-like receptor 9 with DNA-based nanomaterials. *Nano Lett.* **22**, 2506–2513 (2022).
14. Fang, T. et al. Spatial regulation of T-cell signaling by programmed death-ligand 1 on wireframe DNA origami flat sheets. *ACS Nano* **15**, 3441–3452 (2021).
15. Shaw, A. et al. Binding to nanopatterned antigens is dominated by the spatial tolerance of antibodies. *Nat. Nanotechnol.* **14**, 184–190 (2019).
16. Wickham, S. F. J. et al. Complex multicomponent patterns rendered on a 3D DNA-barrel pegboard. *Nat. Commun.* **11**, 5768 (2020).
17. Eklund, A. S., Comberlato, A., Parish, I. A., Jungmann, R. & Bastings, M. M. C. Quantification of strand accessibility in biostable DNA origami with single-staple resolution. *ACS Nano* **15**, 17668–17677 (2021).
18. Goldie, I. & Nachemson, A. Synovial pH in rheumatoid knee-joints. I. The effect of synovectomy. *Acta Orthop. Scand.* **40**, 634–641 (1969).
19. Stevens, C. R., Williams, R. B., Farrell, A. J. & Blake, D. R. Hypoxia and inflammatory synovitis: observations and speculation. *Ann. Rheum. Dis.* **50**, 124–132 (1991).
20. Farr, M., Garvey, K., Bold, A. M., Kendall, M. J. & Bacon, P. A. Significance of the hydrogen ion concentration in synovial fluid in rheumatoid arthritis. *Clin. Exp. Rheumatol.* **3**, 99–104 (1985).
21. Roskams, T., Libbrecht, L., Van Damme, B. & Desmet, V. Fas and Fas ligand: strong co-expression in human hepatocytes surrounding hepatocellular carcinoma; can cancer induce suicide in peritumoural cells? *J. Pathol.* **191**, 150–153 (2000).
22. Li, S. et al. A DNA nanorobot functions as a cancer therapeutic in response to a molecular trigger *in vivo*. *Nat. Biotechnol.* **36**, 258–264 (2018).
23. Liu, S. et al. A DNA nanodevice-based vaccine for cancer immunotherapy. *Nat. Mater.* **20**, 421–430 (2021).
24. Manuguri, S., Nguyen, M. K., Loo, J., Natarajan, A. K. & Kuzyk, A. Advancing the utility of DNA origami technique through enhanced stability of DNA-origami-based assemblies. *Bioconjug. Chem.* **34**, 6–17 (2023).
25. Wang, P. F., Meyer, T. A., Pan, V., Dutta, P. K. & Ke, Y. G. The beauty and utility of DNA origami. *Chem* **2**, 359–382 (2017).
26. Hahn, J., Wickham, S. F. J., Shih, W. M. & Perrault, S. D. Addressing the instability of DNA nanostructures in tissue culture. *ACS Nano* **8**, 8765–8775 (2014).
27. Ponnuswamy, N. et al. Oligolysine-based coating protects DNA nanostructures from low-salt denaturation and nuclease degradation. *Nat. Commun.* **8**, 15654 (2017).
28. Perrault, S. D. & Shih, W. M. Virus-inspired membrane encapsulation of DNA nanostructures to achieve *in vivo* stability. *ACS Nano* **8**, 5132–5140 (2014).
29. Mei, Q. A. et al. Stability of DNA origami nanoarrays in cell lysate. *Nano Lett.* **11**, 1477–1482 (2011).
30. Chandrasekaran, A. R. Nuclease resistance of DNA nanostructures. *Nat. Rev. Chem.* **5**, 225–239 (2021).
31. Schneider, P. et al. Conversion of membrane-bound Fas (CD95) ligand to its soluble form is associated with downregulation of its proapoptotic activity and loss of liver toxicity. *J. Exp. Med.* **187**, 1205–1213 (1998).
32. Algeciras-Schimnich, A. et al. Molecular ordering of the initial signaling events of CD95. *Mol. Cell. Biol.* **22**, 207–220 (2002).
33. Lee, K. H. et al. The role of receptor internalization in CD95 signaling. *EMBO J.* **25**, 1009–1023 (2006).
34. Malyala, P. & Singh, M. Endotoxin limits in formulations for preclinical research. *J. Pharm. Sci.* **97**, 2041–2044 (2008).
35. Hong, E. et al. Structure and composition define immunorecognition of nucleic acid nanoparticles. *Nano Lett.* **18**, 4309–4321 (2018).
36. Namekawa, T., Wagner, U. G., Goronzy, J. J. & Weyand, C. M. Functional subsets of CD4 T cells in rheumatoid synovitis. *Arthritis Rheum.* **41**, 2108–2116 (1998).
37. Gizinski, A. M. & Fox, D. A. T cell subsets and their role in the pathogenesis of rheumatic disease. *Curr. Opin. Rheumatol.* **26**, 204–210 (2014).
38. Reparon-Schuijt, C. C. et al. Secretion of anti-citrulline-containing peptide antibody by B lymphocytes in rheumatoid arthritis. *Arthritis Rheum.* **44**, 41–47 (2001).
39. Okamoto, K. et al. Induction of apoptosis in the rheumatoid synovium by Fas ligand gene transfer. *Gene Ther.* **5**, 331–338 (1998).
40. Zhang, H. et al. Amelioration of collagen-induced arthritis by CD95 (Apo-1/Fas)-ligand gene transfer. *J. Clin. Investig.* **100**, 1951–1957 (1997).
41. Choy, E. H. & Panayi, G. S. Cytokine pathways and joint inflammation in rheumatoid arthritis. *N. Engl. J. Med.* **344**, 907–916 (2001).
42. Smolen, J. S. & Steiner, G. Therapeutic strategies for rheumatoid arthritis. *Nat. Rev. Drug Discov.* **2**, 473–488 (2003).
43. Fullerton, J. N., O'Brien, A. J. & Gilroy, D. W. Pathways mediating resolution of inflammation: when enough is too much. *J. Pathol.* **231**, 8–20 (2013).
44. Elliott, M. R., Koster, K. M. & Murphy, P. S. Efferocytosis signaling in the regulation of macrophage inflammatory responses. *J. Immunol.* **198**, 1387–1394 (2017).
45. Achkar, I. W. et al. Oncogenic role of dysregulated leptin signaling in the pathogenesis of ovarian cancer. *Transl. Med. Commun.* **4**, 1 (2019).
46. Akhtar, S. et al. Cytokine-mediated dysregulation of signaling pathways in the pathogenesis of multiple myeloma. *Int. J. Mol. Sci.* **21**, 5002 (2020).
47. Mehta, M. et al. Cellular signalling pathways mediating the pathogenesis of chronic inflammatory respiratory diseases: an update. *Inflammopharmacology* **28**, 795–817 (2020).

Methods

Materials and reagents

M13mp18 DNA was purchased from New England BioLabs and BIORULER, staple strands and functional strands from Sangon and MTX from Sigma-Aldrich. Immunization-grade bovine type II collagen, complete Freund's adjuvant and incomplete Freund's adjuvant were provided by Chondrex. Sulfosuccinimidyl 4-(*N*-maleimidomethyl) cyclohexane-1-carboxylate (sulfo-SMCC), Tris-(2-carboxyethyl)phosphine hydrochloride (TCEP) and Hoechst 33342 were purchased from Thermo Fisher Scientific, and anti-mouse TNF-α monoclonal antibody from BioXCell. Mouse TNF-α ELISA kit (catalogue no. 1217202), mouse IL-6 ELISA kit (catalogue no. 1210602), mouse IL-1β ELISA kit (catalogue no. 1210122) and mouse TGF-β1 Elisa kit (catalogue no. 1217102) were purchased from DAKEWE. Mouse TNF-α Elisa kit (catalogue no. EK282HS/3-96), mouse IL-6 ELISA kit (catalogue no. EK206HS-96) and mouse IL-1β ELISA kit (catalogue no. EK201BHS-96) were purchased from MULTI SCIENCES. Recombinant anti-CD95 antibody (EPR21088, no. ab216991), recombinant anti-CD95 antibody (EPR5700, no. ab133619), anti-early endosome antigen-1 (EEA1) antibody (no. ab206860), goat anti-rabbit IgG H&L (Alexa Fluor 488, no. ab150077), donkey anti-rabbit IgG H&L (Alexa Fluor 488, no. ab150073) and donkey anti-goat IgG H&L (Alexa Fluor 594, no. ab150132) were purchased from abcam. Phalloidin-iFluor 594 conjugate (catalogue no. 23122) was purchased from AAT Bioquest. Cleaved caspase 8 rabbit monoclonal antibody (catalogue no. 8592, 98134), CD3ε (E4T1B) XP rabbit monoclonal antibody (catalogue no. 78588), CD19 (Intracellular Domain, D4V4B) XP rabbit monoclonal antibody (catalogue no. 90176) and anti-rabbit IgG, horseradish peroxidase-linked antibody (catalogue no. 7074) were provided by Cell Signaling Technology.

Cell lines

A20 is a murine B cell lymphoma line, a gift from H. Liu at the National University of Singapore. A20 cells were maintained in RPMI-1640 medium supplemented with fetal bovine serum (final concentration 10%) and 2-mercaptoethanol (final concentration 0.05 mM). Jurkat cells were obtained from ATCC (clone E6-1, TIB-152) and maintained in RPMI-1640 medium supplemented with fetal bovine serum (final concentration 10%).

Preparation of DNA origami nanosheets

Rectangular DNA origami nanosheets were fabricated by mixing scaffold strand M13mp18 (final concentration 10 nM) with staple strands (final concentration 80 nM) and functional strands with poly-A overhangs (Supplementary Data 1) in TAE-Mg^{2+} buffer (40 mM Tris, 20 mM acetic acid pH 8.0, 2 mM EDTA and 12.5 mM magnesium acetate). The mixture was then heated to 95 °C and annealed by cooling to 25 °C using a Techne Prime thermal cycler (BIBBY), followed by a purification step using Amicon Ultra-0.5 ml 100 kDa centrifugal filters (Millipore).

CD95L-poly-T conjugation

Poly-T strands were conjugated to CD95 ligand (CD95L) by reaction of the terminal thiol group onto the terminal maleimide of CD95L. Soluble CD95L (Acro Biosystems) was reacted with a fivefold molar excess of Sulfo-SMCC for 1 h, then excess sulfo-SMCC was removed using Amicon Ultra-0.5 ml 10 kDa centrifugal filters (Millipore). Meanwhile, thiolated poly-T strands were incubated with a tenfold molar excess of TCEP for 30 min followed by purification (Amicon Ultra-0.5 ml 3 kDa centrifugal filters, Millipore). A fivefold molar excess of poly-T strands was then reacted with maleimide-CD95L overnight at 4 °C. CD95L-poly-T conjugates were purified by Amicon Ultra-0.5 ml 30 kDa centrifugal filters (Millipore) and analysed by SDS polyacrylamide gel electrophoresis.

Fastener preparation

Mixtures of i-motif structures (10 μM) (Supplementary Data 1) in TAE-Mg^{2+} buffer were heated to 95 °C and then annealed by cooling to 25 °C for 2 h.

Preparation of CD95L-loaded DNA origami nanodevice

CD95L-poly-T conjugates were mixed with the DNA origami nanosheet with protruding single-stranded poly-A strands (molar ratio 18:1) in PBS-Mg^{2+} buffer. The mixture was heated to 37 °C then cooled to 25 °C to facilitate annealing. The DNA origami nanodevice was constructed by the addition of a 40-fold molar excess of i-motif-based fasteners to the DNA origami nanosheet. The mixture was heated to 45 °C and then cooled to 25 °C for five cycles to facilitate assembly.

pH-triggered opening and closing of DNA origami nanodevice

For opening characterization the pH value of the buffer solution was adjusted to 6.5 through the addition of acetic acid (10% w/v), followed by incubation of DNA origami nanodevice samples at 37 °C for 30 min. For closing characterization the pH value of the buffer solution was adjusted from 6.5 to 7.4, followed by incubation of samples at 37 °C.

CD95 receptor clustering

Jurkat or A20 cells were treated for 2 h at 37 °C with either NS-empty, sCD95L (40.0 ng ml^{-1}), NS-10 (the equivalent concentration of CD95L, 40.0 ng ml^{-1}) or ND-10 (the equivalent concentration of CD95L, 40.0 ng ml^{-1}) in the culture medium (pH 7.4) or ND-10 (the equivalent concentration of CD95L, 40.0 ng ml^{-1}) in the culture medium (pH 6.5). Cells were then rinsed with PBS and fixed in 4% paraformaldehyde at room temperature. Cells were washed three times with 0.1% Triton X-100 and stained with anti-CD95 antibody overnight at 4 °C. Nuclei were counterstained with Hoechst 33342 and examined by confocal laser scanning microscopy (CLSM) imaging.

CD95 receptor internalization

Jurkat or A20 cells were treated with NS-10 (the equivalent concentration of CD95L, 40.0 ng ml^{-1}) or ND-10 (the equivalent concentration of CD95L, 40.0 ng ml^{-1}) in culture medium (pH 6.5) for 2 h at 37 °C. For dynamin inhibition, Dyngo-4a (Selleckchem, final concentration 30 μM) was added to the medium. Cells were fixed in 4% paraformaldehyde and permeabilized with 0.1% Triton X-100, followed by staining with anti-CD95 and anti-EEA1 antibodies. Samples were washed and treated with secondary antibodies. Finally, nuclei were counterstained with Hoechst 33342 and examined by CLSM imaging.

Caspase 8 activation

Jurkat or A20 cells were treated with NS-empty, sCD95L (40.0 ng ml^{-1}), NS-10 (the equivalent concentration of CD95L, 40.0 ng ml^{-1}) or ND-10 (the equivalent concentration of CD95L, 40.0 ng ml^{-1}) in culture medium (pH 7.4) or ND-10 (the equivalent concentration of CD95L, 40.0 ng ml^{-1}) in culture medium (pH 6.5) for 6 h. Following treatment, cells were fixed in 4% paraformaldehyde, washed with 0.3% Triton X-100 and then stained with cleaved caspase 8 antibody and species-specific secondary antibody. Samples were further counterstained with Hoechst 33342 and examined by CLSM imaging.

In vitro phagocytic clearance by BMDMs

A20 cells were incubated with ND-10 (40.0 ng ml^{-1}) in culture medium (pH 6.5). Following 2 h of incubation, the culture medium was replaced with fresh medium and cells cultured for a further 4 h. BMDMs were then added with coculture for 0.5 h. Cells were harvested to assess phagocytic clearance efficiency. For cytokine profile analysis, BMDMs were cocultured with A20 cells pretreated with NS-empty, NS-10 or ND-10 in culture medium (pH 6.5) for 24 h.

CIA mouse model

Male 8-week-old DBA/1 mice were purchased from Vital River Laboratory Animal Technology Co. and maintained in a pathogen-free animal facility. All animal experiments were performed following guidelines approved by the ethics committee of Fujian Normal University. The CIA mouse model was established by a prime-boost immunization

procedure with certain modifications[48,49]. An equal volume of bovine type-II collagen solution (2 mg ml^{-1}) and complete Freund's adjuvant (4 mg ml^{-1}) was mixed and emulsified; mice were then intradermally injected with 100 µl of this emulsion at the tail base (prime, day 0). Twenty-one days following prime immunization the mice were given a booster immunization of bovine type-II collagen (100 µg) emulsified in incomplete Freund's adjuvant. Mice were examined every other day for signs of joint inflammation. Each paw was scored from 0 to 4 as previously described[50]. In general, most mice started to show features of joint inflammation by days 28–30.

In vivo distribution of DNA origami nanodevice

Both CIA and healthy mice were used to examine in vivo distribution of the DNA origami nanodevice. Functional strands with Cy5.5 fluorophore labelling were used to replace the corresponding original functional strands in the fabrication step. The Cy5.5-labelled DNA origami nanodevice (40 nM, 100 µl) was then intravenously injected into both CIA and healthy mice. Mice were imaged using the IVIS Lumina system at 6, 12, 24 and 48 h post injection. For ex vivo imaging analysis, mice were sacrificed 24 h following injection and the major organs (heart, liver, spleen, lung, kidney) and forelimb and hindlimb were subjected to imaging. CIA mice were used to investigate the conformational transition of the DNA origami nanodevice in response to pH trigger in vivo. The pH-sensitive (w/ Cy5.5 & BBQ650; 40 nM, 100 µl), pH-non-sensitive (w/ Cy5.5 & BBQ650; 40 nM, 100 µl) and pH-sensitive nanodevices (w/ Cy5.5; 40 nM, 100 µl) were intravenously injected into CIA mice. At 4 h post injection, mice were imaged using the IVIS Lumina system and the major organs were subjected to ex vivo imaging.

In vivo biosafety of DNA origami nanodevices

DNA origami nanodevices loaded with CD95L (ND-10) (20 nM, 100 µl) and ND-empty (20 nM, 100 µl) were intravenously injected into healthy mice; 48 h later, blood was collected for biochemical analysis and the liver for histological analysis.

Immunomodulation effect of DNA origami nanodevices

The endotoxin concentration of DNA origami nanodevice samples was measured using the Pierce Chromogenic Endotoxin Quant Kit (Thermo Scientific). We used a standard curve with a range of 0.01–0.1 EU ml^{-1}. DNA origami nanodevice samples were diluted 100-fold to fit within the sensitivity range of the standard curve. ND-empty (20 nM, 100 µl) was intravenously injected into healthy mice. Serum samples were withdrawn from mice at 6, 12, 24 and 48 h. Serum TNF-α, IL-6 and IL-1β were analysed using ELISA kits.

Therapeutic efficacy in CIA mice

The CIA mouse model was established as described above. When mice showed features of joint inflammation they were divided into five groups as follows: PBS (G1), ND-empty (4 nM, 100 µl) (G2), MTX (5.0 mg kg^{-1}) (G3), anti-TNF-α monoclonal antibody (3.0 mg kg^{-1}) (G4) and ND-10 (4 nM, 100 µl) (G5). For short-term therapeutic efficacy evaluation, PBS, MTX, ND-empty or ND-10 was intravenously injected every 3 days for a total of five times. Anti-TNF-α mAb was intraperitoneally administered every 3 days, for a total of five times. The clinical score, paw thickness and body weight of mice were monitored every other day. Following treatment, serum was isolated and subjected to biochemical and cytokine profile analyses. The paws of the mice were collected for microCT imaging. The joints of the forelimb and hindlimb were harvested for H&E and safranin O staining and immunohistochemical and RT–PCR analyses. To investigate long-term therapeutic efficacy, CIA mice were divided into four groups: either PBS, MTX (5.0 mg kg^{-1}), anti-TNF-α mAb (3.0 mg kg^{-1}) or ND-10 (4 nM, 100 µl) was intravenously injected every 3 days, for a total of ten times. Clinical score and paw thickness were monitored every other day following treatment.

Statistical analysis

Data are presented as mean ± s.d. unless otherwise indicated. Sample variance was tested using the *F*-test. Significance between two groups was analysed by two-tailed Student's *t*-test. One-way analysis of variance (ANOVA) with Tukey post hoc test was applied for multiple comparisons. Statistical analysis was performed using GraphPad Prism v.8.0.

Reporting summary

Further information on research design is available in the Nature Portfolio Reporting Summary linked to this article.

Data availability

The data that support the findings of this study are available within the Article and its Supplementary Information files. Source data can be found on figshare at https://doi.org/10.6084/m9.figshare.25111502 (ref. 51). Source data are provided with this paper.

References

48. Brand, D. D., Latham, K. A. & Rosloniec, E. F. Collagen-induced arthritis. *Nat. Protoc.* **2**, 1269–1275 (2007).
49. Zhou, B. et al. Therapeutic effects of a novel BAFF blocker on arthritis. *Signal Transduct. Target. Ther.* **4**, 19 (2019).
50. Wang, H. et al. TACI-ligand interactions are required for T cell activation and collagen-induced arthritis in mice. *Nat. Immunol.* **2**, 632–637 (2001).
51. Li, L. A DNA origami device spatially controls CD95 signalling to induce immune tolerance in rheumatoid arthritis. *figshare* https://doi.org/10.6084/m9.figshare.25111502.v2 (2024).

Acknowledgements

We acknowledge financial support from the National University of Singapore (grant nos. NUHSRO/2020/133/Startup/08, NUHSRO/2023/008/NUSMed/TCE/LOA and NUHSRO/2021/034/TRP/09/Nanomedicine), National Medical Research Council (grant no. MOH-OFIRG23jan-0005), Singapore Ministry of Education (grant no. MOE-000387-00), National Research Foundation (grant no. NRF-000352-00), National Natural Science Foundation of China (grant nos. NSFC 82202311, 62288102, 82302356 and 22274081), Science Foundation of Fujian Normal University (grant no. Y07204080K13) and Natural Science Foundation of Jiangsu Province, Major Project (grant no. BK20212012). We thank H. Liu at the National University of Singapore for providing A20 cells. We thank X. Song at the West China School of Public Health and West China Fourth Hospital, Sichuan University for help with confocal microscopy imaging. We thank B. Zhou at the State Key Laboratory of Biotherapy and Cancer Center, West China Hospital, Sichuan University for help with establishing the CIA model. We thank Guangzhou Sagene Biotech Co., Ltd. for help in making the pattern diagrams.

Author contributions

X.C., J.C., Z.Y., L.L., J.Y., W.M. and L.T. conceived and designed the experiments. L.L., J.Y., W.M., L.T. and L.Y. performed experiments and wrote the manuscript. J.Z., T.D. and Y.Z. performed data analysis. X.C., J.C. and Z.Y. supervised the entire project. L.W. and C.F. conducted proofreading of the manuscript. All authors discussed the results and commented on the manuscript.

Competing interests

The authors declare no competing interests.

Additional information

Extended data is available for this paper at https://doi.org/10.1038/s41563-024-01865-5.

Supplementary information The online version contains supplementary material available at https://doi.org/10.1038/s41563-024-01865-5.

Correspondence and requests for materials should be addressed to Zhen Yang, Jie Chao or Xiaoyuan Chen.

Peer review information *Nature Materials* thanks Maartje Bastings, Mauro Perretti, Marcus Peter and Liangfang Zhang for their contribution to the peer review of this work.

https://doi.org/10.1038/s41563-024-01865-5

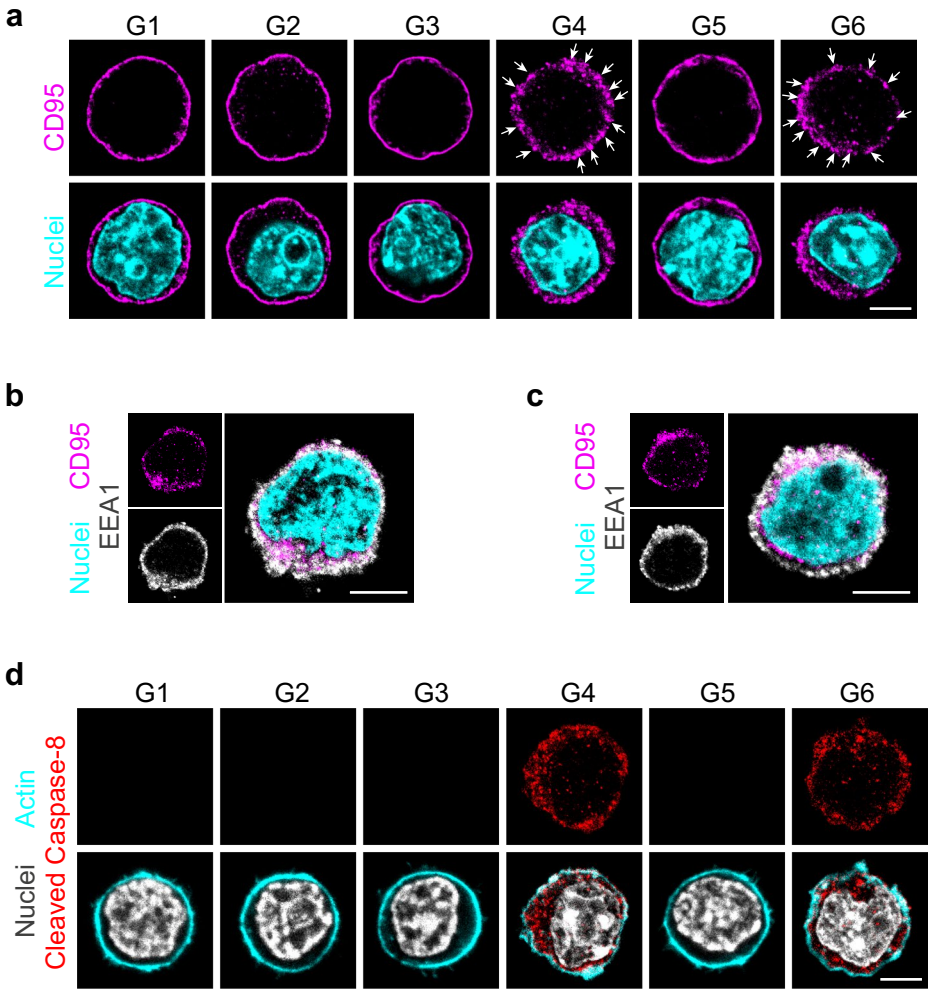

Extended Data Fig. 1 | The spatial arrangement of the CD95L array directs the activation of CD95 signaling in Jurkat cells. a, Clustering of CD95 receptors in Jurkat cells 2 h following treatment with NS-empty (G2), sCD95L (G3), NS-10 (G4), ND-10 in the culture medium (pH 7.4) (G5), ND-10 in the culture medium (pH 6.5) (G6). Untreated (G1); Scale bar, 5 µm. The experiment was performed three times with similar results. (**b**, **c**), Colocalization of CD95 with the endosomal marker-early endosome antigen (EEA1) following NS-10 stimulation (**b**) or ND-10 stimulation in the culture medium (pH 6.5) (**c**). Scale bar, 5 µm. The experiment was performed three times with similar results. **d**, Immunocytochemistry analysis of Cleaved Caspase-8 in Jurkat cells 6 h following treatment with NS-empty (G2), sCD95L (G3), NS-10 (G4), ND-10 in the culture medium (pH 7.4) (G5), ND-10 in the culture medium (pH 6.5) (G6). Untreated (G1); Scale bar, 5 µm. The experiment was performed three times with similar results.

https://doi.org/10.1038/s41563-024-01865-5

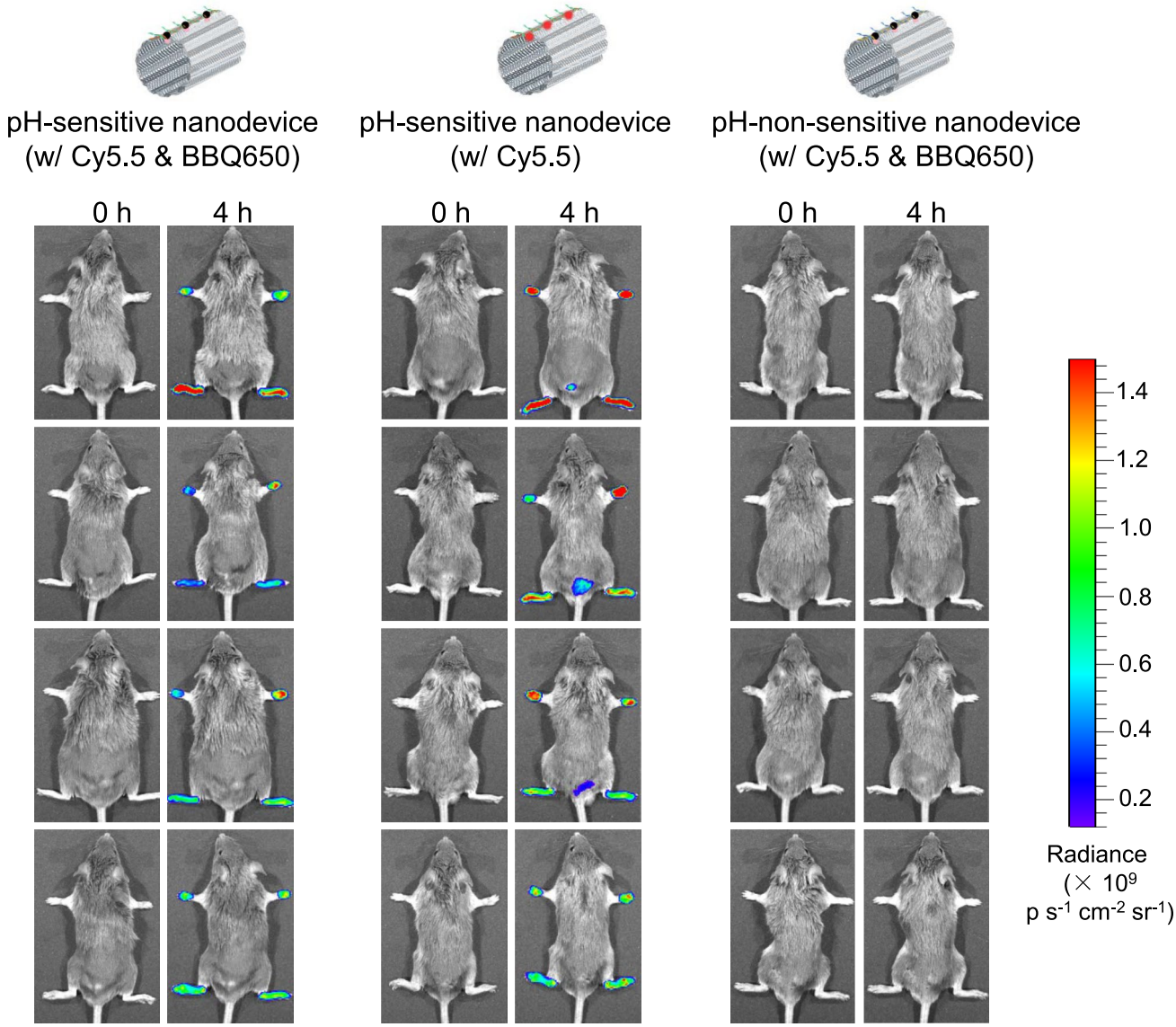

Extended Data Fig. 2 | DNA origami nanodevice exhibits conformational transition in response to pH trigger in vivo. Representative in vivo fluorescence images of CIA mice after intravenous injection with pH-sensitive nanodevice with i-motif-based fasteners labeled with both Cy5.5 fluorophore and BBQ650 quencher (w/ Cy5.5 & BBQ650), pH-sensitive nanodevice with i-motif-based fasteners labeled with Cy5.5 fluorophore (w/ Cy5.5), or pH-non-sensitive nanodevice with the pH-non-sensitive fasteners labeled with both Cy5.5 fluorophore and BBQ650 quencher (w/ Cy5.5 & BBQ650).

https://doi.org/10.1038/s41563-024-01865-5

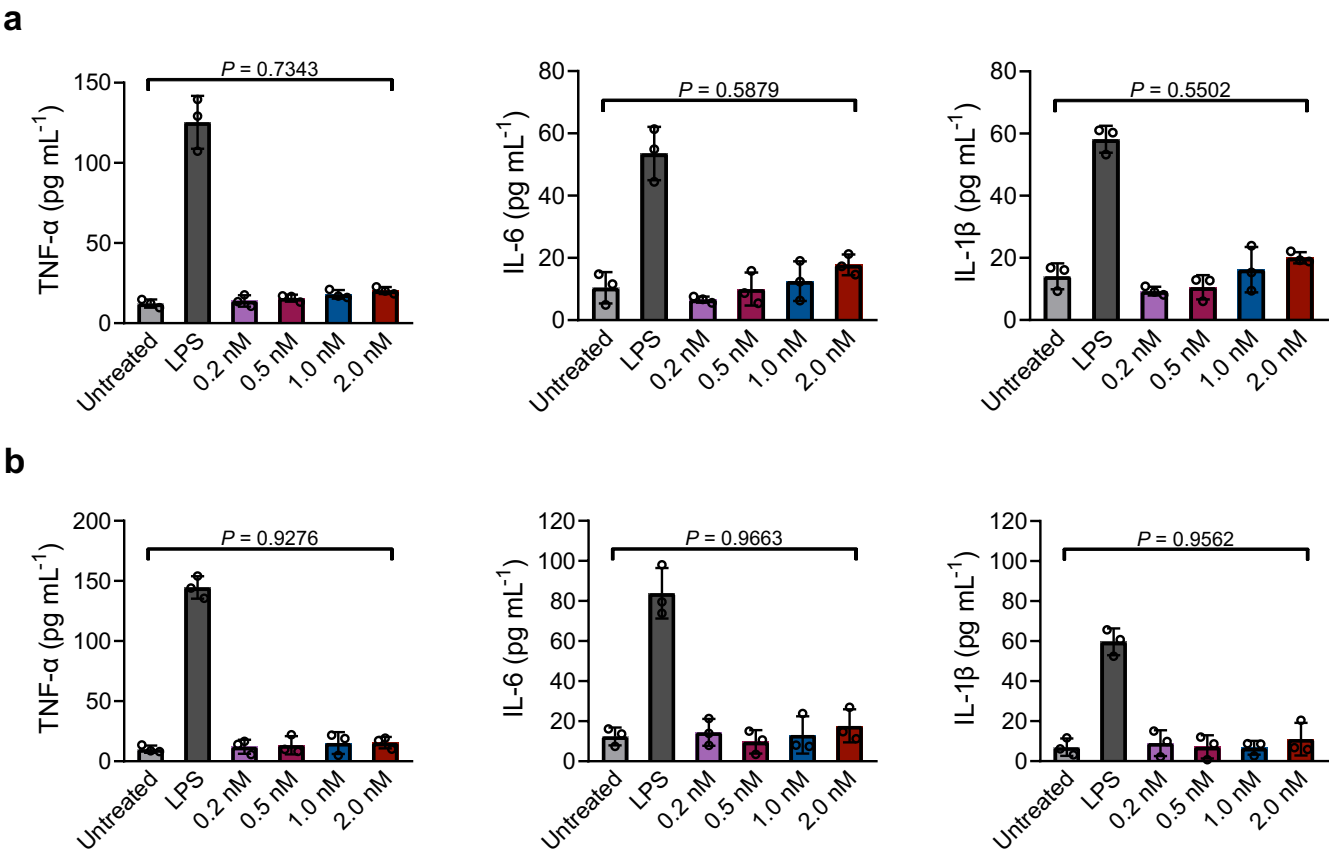

Extended Data Fig. 3 | Designer DNA origami shows minimal immunomodulation potential. (**a**, **b**) Concentration of TNF-α, IL-6, and IL-1β in the supernatants of RAW 264.7 cells (**a**) and BMDMs (**b**) following ND-empty treatment at indicated concentration. LPS (lipopolysaccharide, Invitrogen) was used as a control. n = 3 biologically independent samples per group. Note that the cytokine concentrations in some samples were below the threshold of the assay range and they were determined by extrapolating from the standard curve. Data presented as means ± s.d. Statistical significance was calculated via One-way ANOVA with Tukey post-hoc test (**a**, **b**).

https://doi.org/10.1038/s41563-024-01865-5

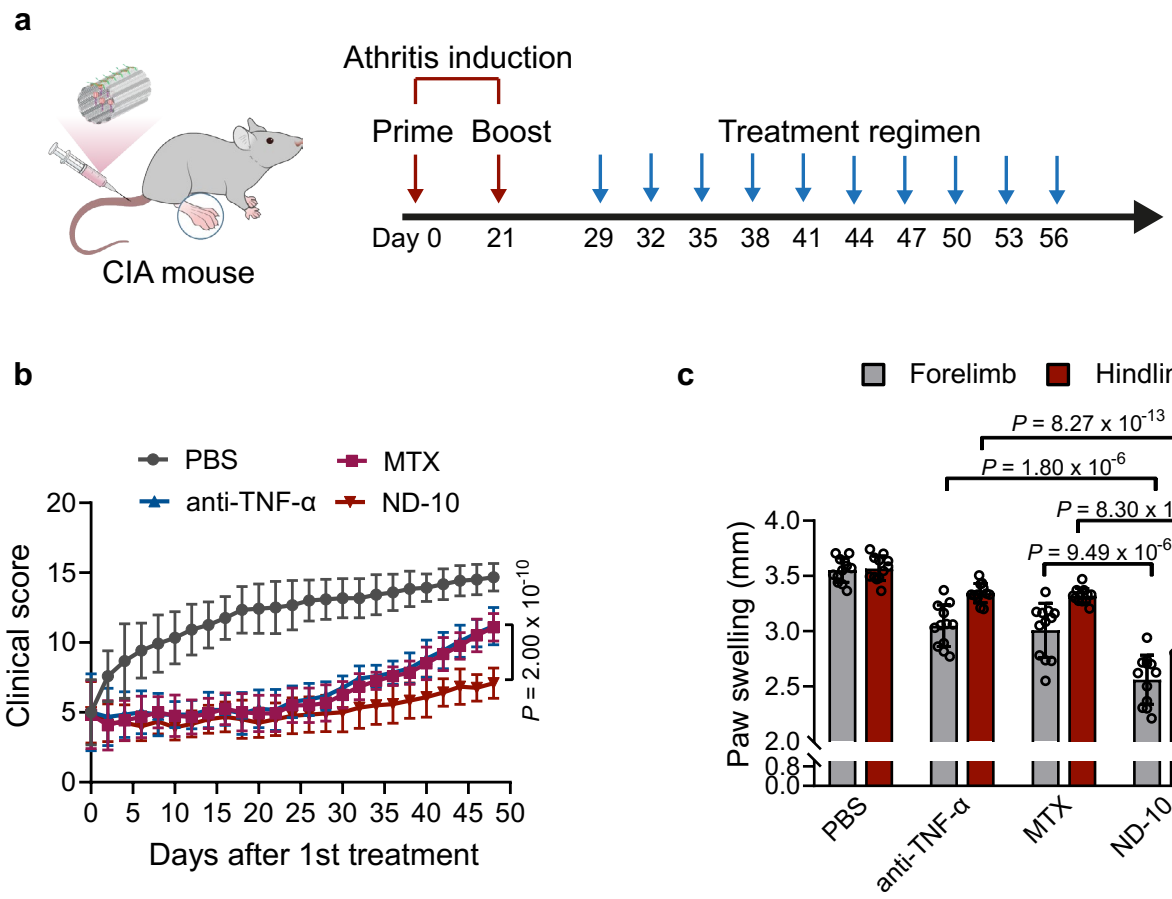

Extended Data Fig. 4 | Designer DNA origami yields long-term therapeutic efficacy in CIA mice. a, Schematic illustration of the long-term treatment regimen. **b**, Clinical arthritis scores of the CIA mice following indicated treatments. n = 12 biologically independent mice per group. **c**, The paw swelling measurement of the CIA mice following indicated treatments. n = 12 biologically independent mice per group. Data presented as means ± s.d. Statistical significance was calculated via One-way ANOVA with Tukey post-hoc test (**b**, **c**). The experiment was performed twice with similar results.

nature portfolio

Corresponding author(s): Zhen Yang, Jie Chao and Xiaoyuan Chen

Last updated by author(s): Jan 30, 2024

Reporting Summary

Nature Portfolio wishes to improve the reproducibility of the work that we publish. This form provides structure for consistency and transparency in reporting. For further information on Nature Portfolio policies, see our Editorial Policies and the Editorial Policy Checklist.

Statistics

For all statistical analyses, confirm that the following items are present in the figure legend, table legend, main text, or Methods section.

n/a	Confirmed	
☐	☒	The exact sample size (*n*) for each experimental group/condition, given as a discrete number and unit of measurement
☐	☒	A statement on whether measurements were taken from distinct samples or whether the same sample was measured repeatedly
☐	☒	The statistical test(s) used AND whether they are one- or two-sided *Only common tests should be described solely by name; describe more complex techniques in the Methods section.*
☒	☐	A description of all covariates tested
☐	☒	A description of any assumptions or corrections, such as tests of normality and adjustment for multiple comparisons
☐	☒	A full description of the statistical parameters including central tendency (e.g. means) or other basic estimates (e.g. regression coefficient) AND variation (e.g. standard deviation) or associated estimates of uncertainty (e.g. confidence intervals)
☐	☒	For null hypothesis testing, the test statistic (e.g. *F*, *t*, *r*) with confidence intervals, effect sizes, degrees of freedom and *P* value noted *Give P values as exact values whenever suitable.*
☒	☐	For Bayesian analysis, information on the choice of priors and Markov chain Monte Carlo settings
☒	☐	For hierarchical and complex designs, identification of the appropriate level for tests and full reporting of outcomes
☒	☐	Estimates of effect sizes (e.g. Cohen's *d*, Pearson's *r*), indicating how they were calculated

Our web collection on statistics for biologists contains articles on many of the points above.

Software and code

Policy information about availability of computer code

Data collection	Living Image software (v4.7.2); FV31S-SW Viewer software (v2.3); Microsoft Excel
Data analysis	Graphpad Prism (v8.0) was used for graph preparation and statistical analysis. Flow cytometry data were analysed on FlowJo software (v10; BD Biosciences). Living image software (v4.7.2, Perkin Elmer) was used to analyse fluorescence images

For manuscripts utilizing custom algorithms or software that are central to the research but not yet described in published literature, software must be made available to editors and reviewers. We strongly encourage code deposition in a community repository (e.g. GitHub). See the Nature Portfolio guidelines for submitting code & software for further information.

Data

Policy information about availability of data

All manuscripts must include a data availability statement. This statement should provide the following information, where applicable:

- Accession codes, unique identifiers, or web links for publicly available datasets
- A description of any restrictions on data availability
- For clinical datasets or third party data, please ensure that the statement adheres to our policy

The data that support the findings of this study are available within the Article and its Supplementary Information files. Datasets can be found at https://doi.org/10.6084/m9.figshare.25111502.

Research involving human participants, their data, or biological material

Policy information about studies with human participants or human data. See also policy information about sex, gender (identity/presentation), and sexual orientation and race, ethnicity and racism.

Reporting on sex and gender	N/A
Reporting on race, ethnicity, or other socially relevant groupings	N/A
Population characteristics	N/A
Recruitment	N/A
Ethics oversight	N/A

Note that full information on the approval of the study protocol must also be provided in the manuscript.

Field-specific reporting

Please select the one below that is the best fit for your research. If you are not sure, read the appropriate sections before making your selection.

☒ Life sciences ☐ Behavioural & social sciences ☐ Ecological, evolutionary & environmental sciences

For a reference copy of the document with all sections, see nature.com/documents/nr-reporting-summary-flat.pdf

Life sciences study design

All studies must disclose on these points even when the disclosure is negative.

Sample size	Sample sizes were determined on the basis of estimates from preliminary experiments. Power analysis was not performed but our sample sizes are similar to those reported in previous publications (Nature Nanotech 13, 1182–1190 (2018); Nature Mater 17, 528–534 (2018); Nat. Mater. 20, 421–430 (2021)).
Data exclusions	No sample was excluded from data analysis.
Replication	Experiments were repeated at least twice, unless otherwise stated in the respective figure legend. Replicates were reproducible.
Randomization	Animal groups were randomized by body weight and/or age. Beyond animals, selection of cells for fluorescent images was randomized.
Blinding	Clinical arthritis score and paw swelling measurements were performed by independent researchers who were blinded as to treatment-group assignment. Fluorescence imaging was conducted by independent operators, who were unaware of the treatment conditions. For cell studies, the researchers collecting the data were blinded to treatment/group assignment.

Reporting for specific materials, systems and methods

We require information from authors about some types of materials, experimental systems and methods used in many studies. Here, indicate whether each material, system or method listed is relevant to your study. If you are not sure if a list item applies to your research, read the appropriate section before selecting a response.

Materials & experimental systems

n/a	Involved in the study
☐	☒ Antibodies
☐	☒ Eukaryotic cell lines
☒	☐ Palaeontology and archaeology
☐	☒ Animals and other organisms
☒	☐ Clinical data
☒	☐ Dual use research of concern
☒	☐ Plants

Methods

n/a	Involved in the study
☒	☐ ChIP-seq
☐	☒ Flow cytometry
☒	☐ MRI-based neuroimaging

Antibodies

Antibodies used	Anti-mouse TNF-α monoclonal antibody (BioXCell, cat: BE0058, clone: XT3.11); Recombinant Anti-CD95 antibody [EPR21088] (Abcam,

Antibodies used	cat: ab216991, dilution: 1:100); Recombinant Anti-CD95 antibody [EPR5700] (Abcam, cat: ab133619, dilution: 1:500); Anti-EEA1 Antibody (Abcam, cat: ab206860, dilution: 1:200); Goat Anti-Rabbit IgG H&L (Alexa Fluor® 488) (Abcam, cat: ab150077, dilution: 1:800); Donkey Anti-Rabbit IgG H&L (Alexa Fluor® 488) (Abcam, cat: ab150073, dilution: 1:800); Donkey Anti-Goat IgG H&L (Alexa Fluor® 594) (Abcam, cat: ab150132, dilution: 1:500); Phalloidin-iFluor™ 594 Conjugate (AAT Bioquest, cat: 23122, dilution: 1:1000); Cleaved Caspase-8 (Asp387) (D5B2) XP® Rabbit monoclonal antibody (Cell Signaling Technology, cat: 8592, dilution: 1:800); Cleaved Caspase-8 (Asp374) (E6H8S) Rabbit (Cell Signaling Technology, cat: 98134, dilution: 1:200); CD3ε (E4T1B) XP® Rabbit monoclonal antibody (Cell Signaling Technology, cat: 78588, dilution: 1:200); CD19 (Intracellular Domain) (D4V4B) XP® Rabbit monoclonal antibody (Cell Signaling Technology, cat: 90176, dilution: 1:3000); Anti-rabbit IgG, HRP-linked Antibody (Cell Signaling Technology, cat: 7074, dilution: 1:1000).
Validation	All antibodies were verified by the supplier, and each lot was quality-tested. These antibodies were used based on the instruction of the manufacturers without additional validation. https://www.abcam.com/products/primary-antibodies/fas-antibody-epr21088-ab216991.html; https://www.abcam.com/products/primary-antibodies/fas-antibody-epr5700-ab133619.html; https://www.abcam.com/products/primary-antibodies/eea1-antibody-early-endosome-marker-ab206860.html; https://www.cellsignal.com/products/primary-antibodies/cleaved-caspase-8-asp387-d5b2-xp-rabbit-mab/8592; https://www.cellsignal.com/products/primary-antibodies/cleaved-caspase-8-asp374-e6h8s-rabbit-mab/98134; https://www.cellsignal.com/products/primary-antibodies/cd3e-e4t1b-xp-174-rabbit-mab/78588; https://www.cellsignal.com/products/primary-antibodies/cd19-intracellular-domain-d4v4b-xp-rabbit-mab/90176.

Eukaryotic cell lines

Policy information about cell lines and Sex and Gender in Research

Cell line source(s)	A20 (ATCC) is a murine B cell lymphoma line, which was a gift from Prof. Haiyan Liu at the National University of Singapore. A20 cells were maintained in RPMI-1640 Medium supplemented with fetal bovine serum (final concentration, 10%) and 2-mercaptoethanol (final concentration, 0.05 mM). Jurkat cells were obtained from ATCC (Clone E6-1, TIB-152) and maintained in RPMI-1640 Medium supplemented with fetal bovine serum (final concentration, 10%). RAW 264.7 cells were obtained from ATCC (TIB-71) and maintained in Dulbecco's Modified Eagle's Medium with fetal bovine serum (final concentration, 10%).
Authentication	Cell lines were authenticated by using PCR assays with species-specific primers.
Mycoplasma contamination	Cell lines were tested negative for mycoplasma contamination.
Commonly misidentified lines (See ICLAC register)	No commonly misidentified cell lines were used.

Animals and other research organisms

Policy information about studies involving animals; ARRIVE guidelines recommended for reporting animal research, and Sex and Gender in Research

Laboratory animals	Male 8-week-old DBA/1 mice were purchased from Vital River Laboratory Animal Technology. All mice were housed in 12 light/12 dark cycle at room temperatures ranging between 20 °C and 25 °C with 40-60% humidity.
Wild animals	No wild animals were used in the study.
Reporting on sex	Male.
Field-collected samples	No field-collected samples were used in the study.
Ethics oversight	The animal experiments were carried out in accordance with the guidelines approved by the ethics committee of Fujian Normal University.

Note that full information on the approval of the study protocol must also be provided in the manuscript.

Plants

Seed stocks	N/A
Novel plant genotypes	N/A
Authentication	N/A

Flow Cytometry

Plots

Confirm that:

☒ The axis labels state the marker and fluorochrome used (e.g. CD4-FITC).

☒ The axis scales are clearly visible. Include numbers along axes only for bottom left plot of group (a 'group' is an analysis of identical markers).

☒ All plots are contour plots with outliers or pseudocolor plots.

☒ A numerical value for number of cells or percentage (with statistics) is provided.

Methodology

Sample preparation	For tissue samples, the tissue was first mechanically disrupted from mice, divided into small pieces, and homogenized in cold staining buffer to form single cell suspensions in the presence of digestive enzyme (Collagenase IV (1 mg/ml), deoxyribonuclease (100 µg/ml)). The cell suspension was passed through a 70-µm cell strainer and treated with ACK lysis buffer (Gibco). The single cell suspension was washed with FACS buffer, incubated with anti-CD16/32 antibodies, and then stained with the indicated antibodies.
Instrument	BD Accuri C6 Plus Flow cytometer (BD Biosciences)
Software	FlowJo (v10; BD Biosciences, USA)
Cell population abundance	No purification.
Gating strategy	The cells were first gated based on FSC-A/SSC-A and SSC-A/SSC-H to select for single cells. Single-color and FMO (fluorescence minus one) stains were used to determine positive populations.

☒ Tick this box to confirm that a figure exemplifying the gating strategy is provided in the Supplementary Information.